Breaking Down the Performance Losses in O$_2$-Evolution Stability Tests of IrO$_2$-based Electrocatalysts

Nataša Diklić,[1] Alexandra Beard,[1] Juan Herranz,[1,*,z] Adrian Heinritz,[1] Tianyu Cen,[1,2] Steffen Garbe,[1] Daniel F. Abbott,[1] Mauro Povia,[1] and Thomas J. Schmidt[1,3,**]

[1]*Paul Scherrer Institut, Electrochemistry Laboratory CH-5232 Villigen PSI, Switzerland*
[2]*Paul Scherrer Institut, Bioenergy and Catalysis Laboratory CH-5232 Villigen PSI, Switzerland*
[3]*ETH Zurich, Laboratory for Physical Chemistry, CH-8093 Zurich, Switzerland*

Understanding the deactivation mechanisms affecting the state-of-the-art, Ir oxide catalysts employed in polymer electrolyte water electrolyser (PEWE-) anodes is of utmost importance to guide catalyst design and improve PEWE-durability. With this motivation, we have tried to decouple the contributions of various degradation mechanisms to the overall performance losses observed in rotating disk electrode (RDE) tests on three different, commercial Ir oxide catalysts (pure or supported on Nb$_2$O$_5$). Specifically, we investigated whether these performance decays stem from an intrinsic deactivation of the catalysts caused by alterations in their oxidation state, crystalline structure, morphology and/or Ir-dissolution, and also assessed possible decreases in the catalyst loading caused by the delamination of the materials over the course of these OER-stability tests. Additionally, we also examined recently reported artifacts related to the use of RDE voltammetry for such measurements and found that neither these nor the above mechanisms (or combinations thereof) can cause the totality of the observed performance losses. Beyond these uncertainties, complementary PEWE-tests showed that this apparent RDE-instability is not reproduced in this application-relevant environment.
© 2023 The Author(s). Published on behalf of The Electrochemical Society by IOP Publishing Limited. This is an open access article distributed under the terms of the Creative Commons Attribution 4.0 License (CC BY, http://creativecommons.org/licenses/by/4.0/), which permits unrestricted reuse of the work in any medium, provided the original work is properly cited. [DOI: 10.1149/1945-7111/ace741]

Supplementary material for this article is available online

The sought-after achievement of a net-zero emissions society requires a fast shift from the current energetic reliance on fossil fuels to more sustainable and environmentally friendly energy sources. However, these renewable energies feature an intermittent nature that must be buffered through further developments in energy storage and conversion technologies. In this context, hydrogen is broadly regarded as a key energy carrier (e.g., for its re-electrification in fuel cells or as a feedstock for the chemistry sector), but its environmentally benign production relies on the continued development of polymer electrolyte water electrolysers (PEWEs). To reach the H$_2$-production costs needed to render this technology cost-competitive ($\leqslant$2 USD · kg$^{-1}_{H2}$),[1–3] further improvements in the operative efficiency and costs of PEWEs are urgently needed. For large scale applications (i.e., implying power inputs in the order of the MW per installation), both of these requirements are linked to the oxygen evolution reaction (OER) taking place at PEWE-anodes, since the OER is largely responsible for the device's operative efficiency losses (particularly when thin membranes are employed).[4] Furthermore, the highly-priced iridium oxides (IrO$_2$) used to catalyze this reaction represent a major contributor to the stack cost at this scale.[5] Additionally, the constraints on Ir mining ($<$10 t$_{Ir}$ · year^{-1})[6] combined with the high Ir loadings used in current PEWE-anodes (typically $\approx$ 2 mg$_{Ir}$ · cm^{-2})[7–10] could significantly restrict the installation of PEWE capacity.[6,7] Thus, ongoing research efforts focus on the development of IrO$_x$-catalysts with enhanced OER-activities and that should allow to decrease the amount of noble metal implemented in each device and lessen the efficiency losses associated to this reaction.

One approach to increase the OER-activity and concomitantly reduce the Ir-loading in PEWE-anodes is to use supports that enhance the dispersion of the catalyst, i.e., the fraction of the metal inventory located at the catalyst surface and thus available for the reaction. To evaluate potential candidates for such support function, Han et al.[11] screened for oxides that are electrochemically stable under OER conditions, i.e., at a potential of 2 V vs the reversible hydrogen electrode (V$_{RHE}$) and at pH 0. Based on Pourbaix diagrams, they predicted sufficient stability for MoO$_3$, RuO$_2$, Sb$_2$O$_5$, TeO$_3$, WO$_3$, OsO$_4$, PtO$_2$, IrO$_2$, Nb$_2$O$_5$, ZrO$_2$, Ta$_2$O$_5$ and HfO$_2$, and potentially also for TiO$_2$, MnO$_2$, Cu$_2$O$_3$, GeO$_2$, AgO, SnO$_2$, Tl$_2$O$_3$, PbO$_2$ and Bi$_4$O$_7$. While supports with electronic conductivities $<$1 S·cm^{-1} were considered unsuitable for this task,[11] numerous studies have reported a positive impact of the use of such electrically inert supports on the stability of IrO$_2$- or RuO$_2$-based catalysts without compromising the OER-activity and leading to a concomitant decrease of anode-related costs.[12–15] In this regard, the careful choice of a synthesis method can be used to tune the catalyst architecture as to produce an electrically percolating structure that ultimately allows the implementation of such non-conductive supports. An example of this is found in so called core–shell catalysts, in which the "inert" oxide support occupies the material's core and is covered by a (semi-)continuous shell of electrically conductive and OER-active catalyst (e.g., IrO$_x$). Such an approach has been applied commercially to produce an IrO$_2$-shell/TiO$_2$-core catalyst (referred to as IrO$_2$@TiO$_2$) that has been shown to outperform other Ir-based catalysts that implemented conductive supports.[16] Regarding the latter materials, the use of dopants (e.g., In, Sb or F) to render SnO$_2$ conductive has been shown to have no impact on the materials' OER-activity,[17] and in some cases it even led to a negative effect on catalyst stability.[17] Moreover, among the various oxide supports discussed above, Nb$_2$O$_5$ has been reported to have a positive effect on the OER performance of IrO$_2$,[15] but only a few studies have investigated in greater detail such IrO$_2$/Nb$_2$O$_5$ catalysts.[18–20] Specifically, Terezo et al.[18] examined the influence of the synthesis parameters on the OER-activity and stability of IrO$_2$/Nb$_2$O$_5$, while Zlotorowicz et al.[19] found that the presence of Nb$_2$O$_5$ plays a beneficial role on the activity only when operated at higher temperatures (i.e., 80 °C). Nevertheless, it is still unclear whether Nb$_2$O$_5$ has an effect on the OER performance and stability of IrO$_2$.

Besides for the OER activity, understanding the durability and degradation mechanisms of PEWE-anode catalysts is crucial for the future commercialization of these devices,[21] since their projected

lifetime is expected to be in the order of ≈ 10 to ≈ 20 years.[9,10,22,23] In this respect, the durability of Ir-based materials is highly dependent on the way in which they are synthesized and on their degree of crystallinity. Current PEWEs generally rely on thermally prepared, crystalline IrO_2 based materials that provide a good tradeoff between OER-activity and stability and can be synthesized in large amounts with up-scaled synthesis routes. However, even those highly crystalline materials undergo a slow degradation upon operation,[24,25] especially under intermittent conditions in which times of operation and idle periods are alternated.[26] While previous studies on amorphous IrO_x have established that such OER-activity loss is caused by Ir-dissolution,[25,27–32] lattice oxygen evolution,[33–35] changes in the surface active sites[36–42] and/or in morphology[38,42,43] or crystallinity[20,37,44] during prolonged operation, the reasons for the activity deterioration observed for the rutile-like IrO_2-based commercial materials discussed above remain poorly understood.[36,45] This may partially stem from the fact that OER-catalyst durability is often assessed through rotating disk electrode (RDE) measurements from which the derived results have recently been shown to be affected by artifacts that preclude their comparison with the stability behavior observed in actual PEWE tests.[46–48] This in turn introduces additional complexity to the interpretation of stability results (and inferred deactivation mechanisms) derived from such RDE-tests.

To shed light on these questions, herein we present a detailed investigation of the OER-activity and -stability of a commercial IrO_2 and two niobium-oxide-supported iridium dioxide (IrO_2/Nb_2O_5) catalysts prepared using different Ir-precursors. Specifically, we have performed a systematic study of the performance losses undergone by these three materials during OER stability tests in RDE configuration. While no intrinsic changes of the catalysts' properties were inferred using an array of characterization techniques, slight dissolution of both Nb and Ir and a migration of the catalyst particles during the OER-stability tests were observed for all three materials. Moreover, potential artifacts related to this stability evaluation in RDE were investigated, and the derived results were compared to those obtained in single PEWE-cell measurements. That comparison showed that catalyst durability is largely underestimated when evaluated by means of RDE-tests.

Experimental

Materials.—The catalysts evaluated in this study include a pure IrO_2 as well as two IrO_2/Nb_2O_5 powders. All catalysts (IrO_2 MA 1021 A3, $IrNbO_x$ BRO 0471 A1 and $IrNbO_x$ MA 1001 A1) were provided by Umicore®, and differ in the Ir-precursor used in their synthesis. Namely, IrO_2 MA 1021 A3 and $IrNbO_x$ BRO 0471 A1 were synthesized using the same Ir-precursor and are referred to as "IrO_2 (A)" and "IrO_2/Nb_2O_5 (A)" in what follows, while for the synthesis of $IrNbO_x$ MA 1001 A1 another precursor was used, and it is therefore labelled "IrO_2/Nb_2O_5 (B)." Notably, both supported catalysts contain ≈ 75 wt% Ir (75.1 vs 74.1 wt% Ir for IrO_2/Nb_2O_5 (A) vs IrO_2/Nb_2O_5 (B), respectively, as specified by Umicore based on ICP-MS measurements).

Electrochemical characterization.—For the RDE measurements, catalyst inks were prepared by dispersing 10 mg of the catalyst of choice in 4 ml of isopropyl alcohol (HPLC Plus, Sigma Aldrich), 1 ml of ultrapure water (18.2 MΩ·cm, ELGA Purelab) and 20 μL of Nafion solution (≈ 5 wt% Nafion® perfluorinated resin solution, Sigma Aldrich—for an ionomer-to-catalyst mass ratio of ≈ 0.09). Each ink suspension was sonicated for 30 min before depositing a droplet of it on a 5 mm diameter, mirror-polished glassy carbon (GC, SIGRADUR® G, HTW Hochtemperatur-Werkstoffe GmbH) disk embedded in polyetheretherketone (PEEK) RDE tip (Pine Research). This was done using a spin coating method, whereby 5 μL of the ink was dropped on the inverted electrode at a rotating speed of 60 rpm, followed by a gradual increase of the speed up to 500 rpm (requiring ≈ 5 s). A graduated glass cylinder was used to protect the electrode from contamination while drying. The deposition process was repeated twice, yielding a catalyst loading of ≈ 100 μg_{cat}·cm^{-2} (corresponding to Ir-loadings of ≈ 87, ≈ 76 and ≈ 75 μg_{Ir}·cm^{-2} for IrO_2 (A), IrO_2/Nb_2O_5 (A) and IrO_2/Nb_2O_5 (B), respectively). The drying of the first deposited layer lasted ≈ 15 min, while ≈ 20 min were needed for the second layer. For the measurements using a polycrystalline gold disk ($\geqslant 99\%$ Au—Pine Research Instruments) as the catalyst substrate the preparation procedure was the same, except that prior to spin coating deposition on this Au substrate, the Au disk was electrochemically cleaned by cyclic volammetry between 0.13 and 1.60 V$_{RHE}$.

The RDE-assessment of the OER activity and stability of the various IrO_2-based catalysts presented in this study was performed in a three-electrode glass cell (Pine Research Instrumentation). The glassware had been previously cleaned in a 3:1 mixture of 95%–97% H_2SO_4 (EMSURE®, Supelco) and 30% H_2O_2 (EMSURE®, Supelco) overnight, and boiled in ultrapure water at least three times. All measurements were performed at room temperature, using 0.1 M $HClO_4$ electrolyte (made from 60% KANTO Chemical CO. or 70% VERITAS double distilled GFS Chemicals®) saturated with synthetic air (PanGas, 5.6). A Hg/HgSO$_4$ electrode (RE-2CP, BAS Inc., Japan) pre-calibrated against the reversible hydrogen electrode in the same electrolyte and a gold mesh (GoodFellow, 99.9%) held in separated glass compartments were used as reference and counter electrodes, respectively.

To evaluate the catalyst's OER activity, polarization curves were derived from chronoamperometric measurements in which the potential was gradually stepped from 1.0 to 1.56 V$_{RHE}$ while holding for 1 min at each potential and continuously rotating the electrode at 1600 rpm. The current in these polarization curves corresponds to the last point in each of these potential steps. Electrochemical impedance spectroscopy measurements were recorded at 1.00 V$_{RHE}$ in a frequency range from 1 MHz to 1 Hz with 6 points per decade in logarithmic spacing (37 points in total) and 10 mV amplitude. The high frequency resistance was used for the ohmic drop correction of the polarization curves. Additionally, cyclic voltammograms (CVs) were recorded before and after the polarization curve measurements to evaluate potential surface changes. These CV measurements were performed between 1.0 and 1.4 V$_{RHE}$ at 50 and 10 mV s^{-1}.

The materials' stability was examined via an accelerated stress test (AST) consisting of 500 cycles alternating 10 s potential holds at 1.0 and 1.6 V$_{RHE}$ while rotating the electrode at 2900 rpm. This electrode rotation speed is higher than that used in the recording of polarization curves (1600 rpm $-vide$ $supra$), and was applied as a means to aid in the removal of O_2 bubbles in this longer electrochemical measurements. For showcasing the results of these stability tests, the current read at the last point of the 1.6 V$_{RHE}$ hold in each 100th step was normalized with regards to the beginning-of-test value (corresponding to cycle number 0). Additionally, CVs and impedance spectra (in the range from 200 kHz to 100 mHz) were also recorded every 100 cycles.

A flow cell setup described elsewhere[49] was used to examine the changes in the catalysts' (surface) oxidation state via in situ X-ray diffraction (XRD), post mortem X-ray photoelectron spectroscopy (XPS) and transmission electron microscopy (TEM, see below for more information on these techniques). Electrodes were prepared by manually spray coating inks on pre-cut pieces of gold-coated Kapton® foil (DuPont Kapton® 200RS100), as described elsewhere.[49] The ink compositions for working- and counter-electrodes are the same as in Ref. [50] and the final loadings of IrO_2/Nb_2O_5 (B) in the working electrode and of Black Pearls 2000 carbon black on the counter electrode were ≈ 2.5 to 3.5 mg$_{cat}$·cm^{-2} vs ≈ 2 mg$_C$·cm^{-2}, respectively. The ionomer-to-catalyst mass ratios were 0.17 vs 0.44 for working- vs counter-electrodes, respectively. During the in situ measurement, the flow of 0.1 M $HClO_4$ (prepared from 60% KANTO Chemical CO.) was controlled by a syringe pump (Legato® 210, KD Scientific) operated at 0.2 ml·min^{-1}.

For the single cell PEWE measurements, 25 cm^2 MEAs were prepared by spray-coating the catalysts of choice on a Nafion® N117

membrane (Ion Power) using an automated spray coating machine (Sonotek, ExactaCoat) with the membrane-holder heated to 50 °C and using the same parameters as described in Refs. 51, 52 Specifically, the spraying nozzle was set to 10 mm height and its moving speed was 80 mm · s^{-1}, while the inks were sprayed at a flow rate of 0.005 ml · min. The anode catalyst ink was prepared by mixing 751.7 mg of IrO$_2$/Nb$_2$O$_5$ (B), 1.911 ml of Nafion solution (Ion Power D521, 5 wt% Nafion®, for an ionomer-to-catalyst mass ratio of 0.11[53,54]), 1.248 ml of isopropyl alcohol (HPLC Plus, Sigma Aldrich) and 3.892 ml of ultrapure water (18.2 MΩ·cm, ELGA Purelab) and sonicating the resulting suspension for 30 min Likewise, the cathode catalyst ink was prepared by sonicating a mixture of 432.9 mg of a platinum on carbon catalyst (47% Pt/C − TEC10E50E, Tanaka Kikinzoku Kogyo), 6.432 ml of isopropyl alcohol (HPLC Plus, Sigma Aldrich), 3.960 ml of milliQ water and 3.664 ml of Nafion® solution (Ion Power D521, 5 wt% Nafion®, for an ionomer to carbon mass ratio of 0.7). In order to determine the catalyst loading, a reference piece of polytetrafluoroethylene (PTFE) sheet was sprayed simultaneously and checked periodically. The Pt loading on the cathode side was 0.4 mg$_{Pt}$ · cm^{-2}, while the Ir loading on the anode was 2 mg$_{Ir}$ · cm^{-2}. The resulting membrane electrode assemblies (MEAs) were sandwiched between a commercial, sintered-titanium porous transport layer (PTL, Sika T10, GKN Sinter Metal Filters) of 1 mm thickness on the anode side and a carbon gas diffusion layer (GDL, 2050A-6060, SPECTRACARB) of 1.5 mm thickness on the cathode.

The MEAs were tested in a home-built electrolysis test bench described elsewhere.[51] The tests were performed at 60 °C feeding ultrapure water (18.2 MΩ·cm). The water was circulated with a flow rate of 85.6 ml · min^{-1}. The cell was conditioned by performing a 12 h current density hold at 2 A · cm^{-2}. After conditioning, the current density was held at 0.008 A · cm^{-2} for 30 min to stabilize the cell's potential and temperature. Following this step, polarization curves were acquired by performing 10 s holds at current densities between 0.008 and 3 A •cm^{-2}, increasing the steps as reported in Ref. 51 Cyclic voltammograms were recorded in the potential range between 1.0 and 1.4 V to determine the catalyst capacitance while feeding 400 ml · min^{-1} H$_2$ (PanGas, 4.5) to the cell's cathode. Subsequently, impedance spectra were recorded in the range between 100 mHz and 100 kHz. After this initial characterization, the stability of the anode catalyst was evaluated using an AST protocol similar to the one applied in the RDE configuration. While the lower potential hold in each cycle was set to 1.0 V, the upper cell potential was set to 1.889 V (see Fig. S1 and Supplementary Note 1 for more details). Additionally, a full polarization curve was recorded every 100 cycles.

Physicochemical characterization.—The electrical conductivity of the materials was assessed by four-wire impedance spectroscopy measurements at room temperature. For this, the powders were placed in a measurement die with a geometric area of 0.785 cm^2 and pressed under a load of 0.6 MPa. After 2 min, the thickness of the pressed powder was measured, and an impendence spectroscopy measurement was performed at the open circuit applying a 2 mV amplitude perturbation in a frequency range between 100 kHz and 100 mHz. This measurement was repeated three times for each material with different thicknesses.

Nitrogen adsorption/desorption experiments were performed to determine the surface area of the materials, which was derived from the Brunauer–Emmett–Teller (BET) equation based on N$_2$-adsorption isotherms (Autosorb-1, Quantachrome Instruments, Boynton Beach, FL, USA) in the p/p$_0$ range between ≈0.05 and ≈0.3. The samples were outgassed overnight at 60 °C prior to these measurements.

XRD measurements were performed using a Smart Lab Rigaku system equipped with a copper rotating anode as the X-ray source. The diffraction patterns of the powders were recorded in Bragg Brentano mode ($\theta/2\theta$), with the source operating at 160 mA and 40 kV. As this configuration forms a divergent polychromatic beam,

a K filter (made of Nickel) was placed in the secondary optics (i.e., in front of the detector) to remove copper-K$_\beta$ radiation. For those measurements an SC70 point detector was employed. in situ XRD was performed using cross beam optics (CBO) in parallel beam mode, where a graphite parabolic mirror is used to create the parallel beam and, at the same time, to remove copper-K$_\beta$ radiation. For such measurements, a 10 mm slit was used to reduce the size of the parallel X-ray beam. The diffracted X-ray photons were collected using a Rigaku HyPix3000 detector between 15 and 60 deg, with a scan step of 0.05 deg and a scan speed of 1.52954 deg min^{-1}, translating in a collection time of ≈30 min The electrochemical flow cell was fitted in a modified sample holder and its geometry required a so called "2θ" measurement mode, where the X-ray source stays fixed and only the detector scans through the chosen 2θ angles.

Information about the chemical state of Ir at the catalysts' surface was obtained by X-ray photoelectron spectroscopy (XPS). These measurements were performed using a VG ESCALAB 220iXL spectrometer operated with a monochromatic Al Kα source (15 kV/ 150 W). Charging effects were corrected by setting the binding energy of the C 1s peak maximum to an energy of 284.8 eV. The analysis of the spectra was carried out using Casa XPS software. Background subtraction was performed according to Shirley,[55] while Doniach–Šunjić (DS) and Gaussian Lorenzian sum (SGL) functions were employed to fit the Ir 4f peak, together with Gaussian/ Lorenzian (GL) product functions used for its satellites, as described in Ref. 56 The final line shape was determined from a rutile IrO$_2$ purchased from Sigma Aldrich that has been previously used as the reference sample for Ir^{+4} species[50,56] and for which the acquired Ir 4f spectrum and derived fitting parameters are shown in Fig. S2 and Table SI, respectively.

The morphology of the catalysts was investigated using TEM and scanning electron microscopy (SEM) measurements. TEM images were acquired in a TECNAI F30 operated at 300 kV, and SEM measurements were performed in a Carl Zeiss Ultra55 microscope, using the in-lens detector at an acceleration voltage of 3 to 5 kV. For identical location (IL-) SEM studies, a homemade sample holder was used, as shown in Fig. S3. Electrical contact between the glassy carbon disk and the sample holder was established by connecting a spring inside the RDE tip to the SEM holder with copper tape. An additional strip of the same tape was placed over the edge of the glassy carbon electrode all the way down to the sample holder to improve electrical contact further and thus reduce charging issues (see Fig. S3b for more details).

In order to quantify the amount(s) of species dissolved during the ASTs, the latter were repeated in a miniature glass cell only requiring 9 ml of electrolyte, as to decrease the ratio between volume of electrolyte and catalyst mass. Traces of Ir and Nb cationic species dissolved in the post-AST electrolyte were quantified by inductively coupled plasma mass spectrometry (ICP-MS) using an Agilent 7700x station. Complementarily, X-ray fluorescence (XRF) was employed at the RMS Foundation (Bettlach, Switzerland) in order to determine the catalyst loading on the RDE glassy carbon disks before and after the AST measurements. The instrument was calibrated by drop-casting the ink on glassy carbon disk in order to have 4 different Ir and Nb loadings (i.e., between 0 and ≈180 μg$_{Ir}$ · cm^{-2} and 0 to ≈25 μg$_{Nb}$ · cm^{-2}, respectively). Linear fitting was used to generate a calibration line for either species. For the quantification of Ir and Nb, two different electrodes needed to be prepared, one for estimating their quantities before the AST and the other one for performing XRF quantification after the AST.

Results and Discussion

Structural characterization.—Although Nb$_2$O$_5$ is known to be an insulating material,[57,58] the electrical conductivity of the IrO$_2$/Nb$_2$O$_5$ catalysts is only ≈40% lower compared to that of the unsupported IrO$_2$. More precisely, while the measured conductivities of the IrO$_2$/Nb$_2$O$_5$ (A) and IrO$_2$/Nb$_2$O$_5$ (B) catalysts are 7.0 ± 0.3 vs 7.0 ± 0.8 S·cm^{-1}, respectively, the conductivity of the unsupported

IrO$_2$ (A) sample is 11.8 ± 0.6 S·cm^{-1} (see summarized values in Table I). Notably, the latter value is also comparable to the 11.0 ± 0.5 S·cm^{-1} that was measured through the same experimental approach on a commercial IrO$_2$/TiO$_2$ catalyst that has been featured in multiple PEWE studies (see Refs. 8, 10 and 26). Most importantly, this similarity indicates that the coverage of the insulating Nb$_2$O$_5$ support with conductive IrO$_2$ is sufficiently high to provide a (semi)continuous charge percolation network that assures the conduction of electric current along these hybrid materials, similar as previously described for IrO$_2$/TiO$_2$.[59]

Following this important verification, Fig. 1 shows a comparison of the XRD patterns of the same three materials. IrO$_2$/Nb$_2$O$_5$ (B) features diffraction peaks typical for the rutile IrO$_2$ phase (ICSD collection code 81028), while pure IrO$_2$ (A) and IrO$_2$/Nb$_2$O$_5$ (A) contain residual traces of metallic Ir (ICSD collection code 64992—see diffraction features at 2θ-values of ≈41 and ≈48°) that are further discussed below in the context of these materials' XPS results. Moreover, no peaks related to Nb$_2$O$_5$ (see Fig. S4 for reference patterns) are present on any of the materials' XR-diffractograms. This may be the result of a combination of several factors, including (i) a low degree of crystallinity in this Nb-oxide phase, (ii) its relatively low concentration, and/or (iii) the overlap of its diffraction peaks with those of the preponderant IrO$_2$-phase.

The surface oxidation state of both as-synthesized catalysts was evaluated using XPS. As shown in Fig. 2a, the Ir 4f peak in IrO$_2$/Nb$_2$O$_5$ (A) is shifted by ≈0.1 eV towards higher binding energies compared to IrO$_2$/Nb$_2$O$_5$ (B), which could be interpreted as a sign of the presence of reduced, Ir^{+3} species in IrO$_2$/Nb$_2$O$_5$ (A).[56] Considering the XRD results discussed above, though, one would expect an energy shift towards lower binding energies, since IrO$_2$/Nb$_2$O$_5$ (A) contains metallic Ir that would additionally cause a distortion of the Ir 4f doublet. However, such an effect is not observed if the Ir 4f peaks of the two samples are energy-aligned (see Fig. 2b), and instead no differences in their peak shapes can be inferred. This suggests that the Ir in the surface of both catalysts is in the same oxidation state, and that the slight binding energy shift discussed above may be caused by imprecisions in the calibration of the spectra, which relies on the binding energy of an adventitious C 1 s peak (*vide supra*) known to be imprecise due to the undetermined composition of the species contributing to this signal.[60] Finally, the deconvolution of the spectra displayed in Figs. S5a and S5b confirms that surface Ir is in a + 4 oxidation state and that no metallic Ir is present on either of the catalysts' surfaces (see Tables SII and SIII for more details on peak deconvolution). Thus, this indirectly implies that the metallic Ir observed in the XRD pattern of the IrO$_2$/Nb$_2$O$_5$ (A) sample (see Fig. 1) must be buried within its bulk, and is therefore not proved by surface-sensitive XPS.

As for the catalysts' morphology, the SEM images in Fig. S6. show that while IrO$_2$/Nb$_2$O$_5$ (B) consists of fluffy aggregates, IrO$_2$/Nb$_2$O$_5$ (A) and IrO$_2$ (A) feature less porous particles. This morphological difference is in line with the materials' surface areas inferred from the N$_2$-sorption measurements, which is > 2-fold higher for IrO$_2$/Nb$_2$O$_5$ (B) (24 m^2·g^{-1}) as compared to IrO$_2$/Nb$_2$O$_5$ (A) and IrO$_2$ (A) (with surface areas of 9 vsvs 5 m^2·g^{-1}, respectively—see Table I). Moreover, as pointed out in Fig. S6b, the IrO$_2$/Nb$_2$O$_5$ (A) sample is inhomogeneous, since large particles with distinguishably flat surfaces are found in particular locations across this catalyst. Energy dispersive X-ray spectroscopy (EDX) performed on different spots of this IrO$_2$/Nb$_2$O$_5$ (A) sample (featured in Fig. S7) unveil that the sample volume around these larger particles possesses a Ir/Nb weight ratio of ≈2 that is significantly higher than the value of ≈25 ± 4 determined when such EDX measurements are performed in other spots devoid of such aggregates. Moreover, the latter value is in turn ≈2-fold larger than the Ir/Nb weight ratio of ≈12.1 ± 0.2 found by EDX of the visually homogeneous IrO$_2$/Nb$_2$O$_5$ (B) catalyst, that is in line with the ratio of ≈ 10.5 derived from the manufacturer's ICP-MS measurements (see the Experimental section for details), as shown on Fig. S8. We believe that this inconsistency is not intrinsically related to a higher Ir-

content in the IrO$_2$/Nb$_2$O$_5$ (A) catalyst compared with IrO$_2$/Nb$_2$O$_5$ (B), but to the fact that (as indicated by the SEM measurements discussed above) the large and flat particles in parts of the former sample correspond to Nb$_2$O$_5$ completely devoid of IrO$_2$, and thus the other regions covered with IrO$_2$ (and analyzed in our EDX measurements) feature a proportionally higher content of this catalytic material.

RDE assessment of the catalysts' OER performance and stability.—Following this assessment of the catalysts' bulk and surface properties, the materials were electrochemically characterized by cyclic voltammetry within potential windows of 0.1 to 1.4 or 1.0 to 1.4 V$_{RHE}$, respectively. As shown in Fig. S9, the CVs recorded on the IrO$_2$/Nb$_2$O$_5$ (B) sample feature a ≈2- vs ≈4-fold larger double layer capacitance than those of IrO$_2$/Nb$_2$O$_5$ (A) and IrO$_2$ (A), respectively, which is in agreement with the differences in surface areas (SAs) inferred from the N$_2$-sorption measurements discussed above (see also Table I). This relation among variables is quantitatively confirmed when considering the CVs recorded in a potential window of 1.0 to 1.4 V$_{RHE}$. Interestingly, a linear relation between the corresponding double layer capacitive charges inferred from the CVs measured in the range between 1.0 and 1.4 V$_{RHE}$ and their SAs derived from the N$_2$-sorption measurements (see Fig. S10a) is found. Moreover, this SA vs charge relation is also consistent with the results presented in previous studies by our group on Ir-oxides synthesized via the Adams fusion method,[36,38] as shown in Fig. S10b. Looking at the CVs recorded in a broader potential window (0.1 to 1.4 V$_{RHE}$), the current peaks appearing at ≈0.8 and ≈0.6 V$_{RHE}$ in the CVs of IrO$_2$/Nb$_2$O$_5$ (B) and IrO$_2$ (A), respectively, indicate an Ir^{+3}/Ir^{+4} redox transition[61,62] assignable to the presence of Ir^{+3} species on these catalysts' surfaces. This may appear to contradict the XPS results presented above, since these samples' Ir 4f spectra could be deconvoluted exclusively using Ir^{+4} components (see Fig. S1 and S5b). However, one must bear in mind that while those voltammetric features are derived from truly interfacial-sensitive electrochemical measurements, the XP-spectra are not selectively representative of the catalysts' topmost layer. Instead, the measured Ir 4f XPS signals arise from ≈5 nm along the samples' thickness, and thus spectral contributions of Ir^{+3} species that may only be present within the catalysts' surface (and potentially featured within submonolayer coverages) can be fully overlapped by that of the Ir^{+4} phase mostly featured along the probed sample depth. Finally, the CV of the IrO$_2$/Nb$_2$O$_5$ (A) sample is rather featureless, and the absence of hydrogen underpotential deposition features (expected at potentials <0.4 V$_{RHE}$)[63,64] in all voltammograms confirms the lack of metallic Ir on all catalysts' surfaces.

Following the recording of polarization curves (see Experimental section for details), the catalysts' OER activity was assessed as the Ir-mass normalized current at a potential of 1.55 V$_{RHE}$ and, as shown in Fig. 3a and Table I, IrO$_2$/Nb$_2$O$_5$ (B) exhibits the highest activity. In order to take into account the effect of the surface area on those activity values, the OER-currents were additionally normalized by the charge extracted from the CVs recorded in the range between 1.0 and 1.4 V$_{RHE}$ (*vide supra*)[36,38] and featured in Fig. S9b. While the integrated charges do not allow for a precise quantification of the samples' electrochemical surface areas, they should be proportional to the surface area in contact with the electrolyte and thus participation in the catalytic process.[36] Also, this metric can be considered as a fair comparison between all three materials used in this study, since their surfaces can be regarded as preponderantly consisting of rutile IrO$_2$.[65] Interestingly, once the currents are normalized by this double-layer capacitive charge, the OER-activities of the two catalysts that contain Nb$_2$O$_5$ appear similar (cf Fig. 3b). Therefore, their surface-specific OER- activity is not sensitive to the type of precursor used in their synthesis, and the differences in mass-normalized activity discussed above can be exclusively ascribed to the higher surface area of IrO$_2$/Nb$_2$O$_5$ (B). On the other hand, this charge-normalization also unveils that pure IrO$_2$ (A) possesses the highest surface-specific, intrinsic OER-

Table I. Summary of the physicochemical and electrochemical parameters derived from the conductivity, N$_2$-sorption and electrochemical measurements performed on the three materials included in this study.

Catalyst	Conductivity/S $\cdot$ cm^{-1}	Surface area/m$^2 \cdot$ g^{-1}	j @ 1.55 V$_{RHE}$/A $\cdot$ g$_{Ir}^{-1}$	j @ 1.55 V$_{RHE}$/A $\cdot$ C^{-1}	Tafel slope/mV $\cdot$ dec^{-1}
IrO$_2$/Nb$_2$O$_5$ (B)	7.0 ± 0.8	24	9.0 ± 1.0	0.66 ± 0.08	47.4 ± 0.6
IrO$_2$/Nb$_2$O$_5$ (A)	7.0 ± 0.3	9	5.0 ± 0.1	0.76 ± 0.03	47.3 ± 0.3
IrO$_2$ (A)	11.8 ± 0.6	5	5.8 ± 0.7	1.5 ± 0.1	46.7 ± 0.8
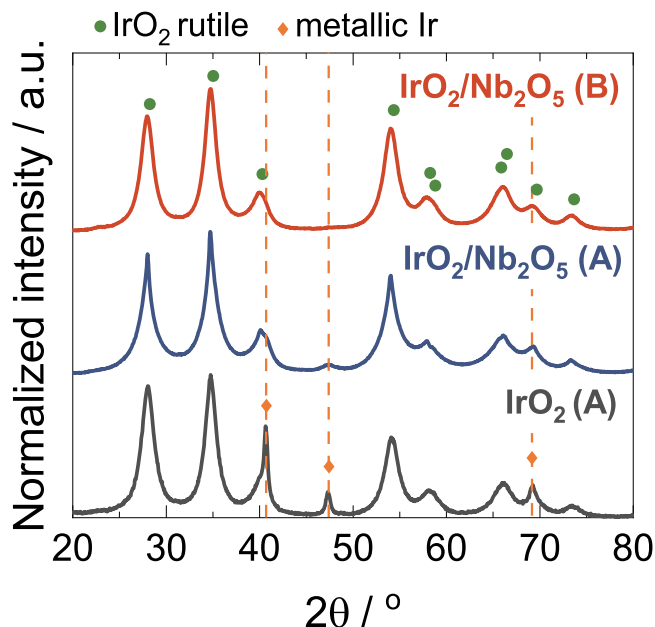
Figure 1. XRD patterns of IrO_2/Nb_2O_5 (B), IrO_2/Nb_2O_5 (A) and pure IrO_2 (A), including the diffraction positions expected for rutile IrO_2 and metallic Ir references (a).

activity. Additionally, the Tafel slope exhibited by all three materials is very similar (≈ 47 mV·dec^{-1}—see Table I), suggesting that the use of Nb_2O_5 as a support does not significantly affect the OER mechanism on this rutile IrO_2-catalysts.

Next, the stability of these catalysts was investigated using an AST that is intended to mimic start/stop events in a PEWE-electrolyser, as described in the above experimental section. While all three catalysts underwent a significant loss of current by the end of the 500 potential steps between 1.0 and 1.6 V_{RHE} (see Fig. 4a), IrO_2/Nb_2O_5 (A) featured the highest stability (having lost $\approx 35\%$ of the initial catalytic performance), followed by IrO_2/Nb_2O_5 (B) and IrO_2 (A) (with ≈ 50 vs $\approx 65\%$ performance losses, respectively). Possible changes in the catalysts' surfaces during this AST were assessed by periodically recording CVs, for which the charge every 100 cycles systematically increased with the test duration/cycle number, as shown in Fig. 4b.

Degradation mechanisms.—In order to understand these differences in stability and increased capacitive charge among materials, and to determine whether the Nb_2O_5 support promotes the durability of IrO_2, we conducted a systematic study evaluating the possible reasons for these trends in the course of the AST. Considering the literature, their corresponding OER-current losses must originate from (i) intrinsic surface-deactivation processes (e.g., due to irreversible changes in Ir oxidation state,[36,38,40] crystallinity,[20,37,44] morphology[38,43] and/or Ir-dissolution[25,27–32]) and/or (ii) effects related to the RDE-configuration adopted for this stability measurement (e.g., a decrease of the catalyst loading due to its detachment,[43] or the corrosion of the glassy carbon on which the catalyst was immobilized[46]). Additionally, a series of recent studies have shown that this apparent degradation can stem from the accumulation of micro-/nano- bubbles within the catalyst layer pores, which would shield the corresponding areas of the catalyst and decrease the fraction of its surface participating in the catalytic process. Thus, in Fig. 5 we have visually summarized these mechanisms, their effects and the techniques used to assess them, and in what follows we present a detailed investigation of these processes in which we try to break down their partial contributions to the overall AST-induced current losses undergone by these 3 catalysts.

Starting with the possible sources of intrinsic catalyst degradation, the surface-specific OER-activity of IrO_x-based catalysts is
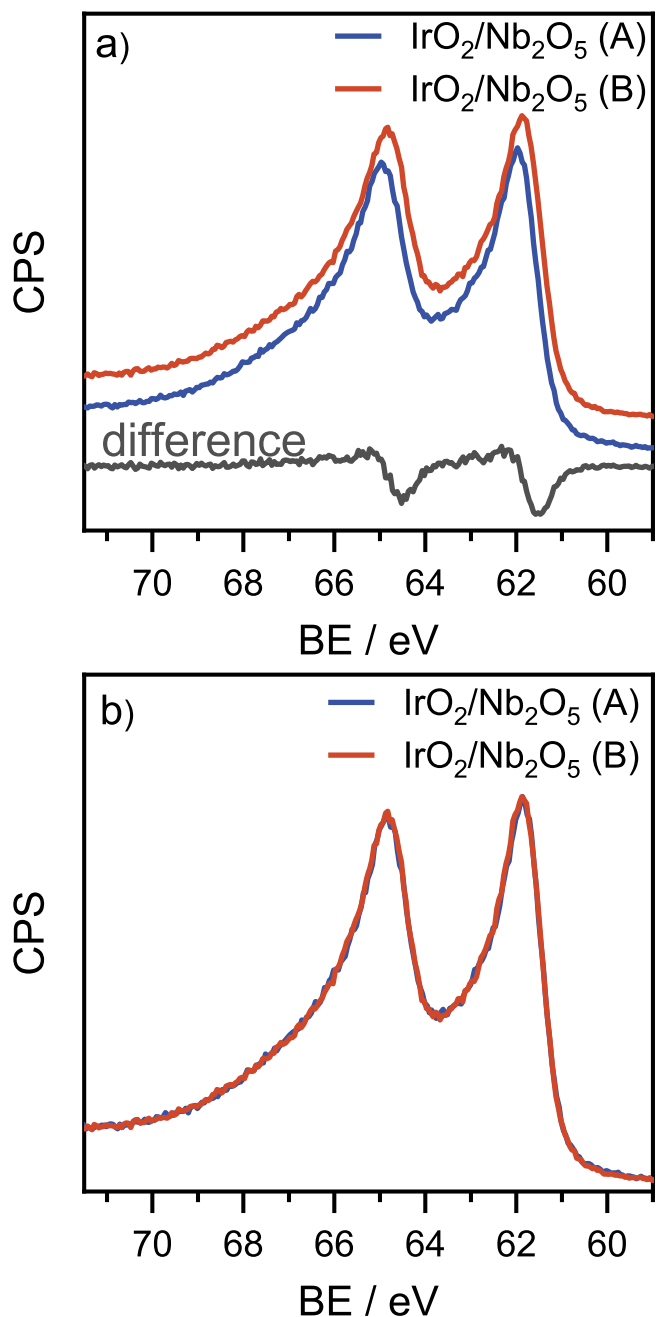

Figure 2. Comparison of the Ir 4f XP-spectra acquired on the IrO_2/Nb_2O_5 (A) and IrO_2/Nb_2O_5 (B) powders, along with their difference spectra (a) and their overlay after alignment of the spectral maxima to the same binding energy (b).

known to be largely dependent on the oxidation state of the Ir-sites on the catalyst's surface.[38,56,66] Therefore, we performed post mortem XPS measurements to assess possible changes in the oxidation state of the catalysts during the AST, but found no changes for either of the catalysts (see Fig. S11). Moreover, the exposure of the catalyst to harsh OER conditions has shown to be detrimental to its crystal structure, with some studies reporting an increase in crystallinity[20,44,67] and others in the structural disorder of the IrO_2-surface[36,38] (perceived, e.g., as an increase in the Ir-O bond distance). To verify this possibility, we performed an in situ XRD measurement (see Experimental section above for details). Since the latter is a bulk technique sensitive to the volume fraction of each phase in the probed materials and the expected operative changes may mostly occur within the catalyst's surface, these measurement
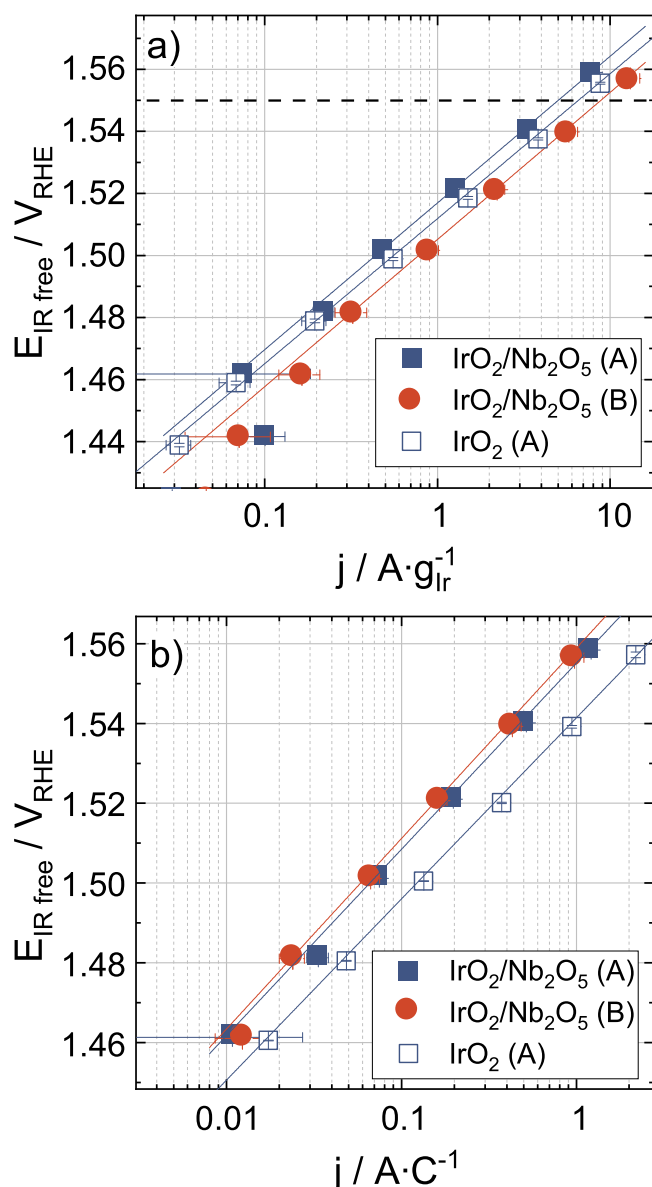
Figure 3. OER-polarization curves recorded on the three $IrO_2(/Nb_2O_5)$ catalysts included in this study, with the currents normalized with respect to the catalysts' mass (a) or to their double layer capacitive charge (b).

Figure 4. Evolution of the OER-current at $1.6\ V_{RHE}$ in the course of the AST (a) and of the corresponding double layer capacitive charges determined from CVs recorded in the range between 1.0 and $1.4\ V_{RHE}$ at $50\ mV \cdot s^{-1}$ (b). Note that both variables appear normalized with respect to their beginning-of-test values.

was carried out on the IrO_2/Nb_2O_5 (B) sample, which is the material with the largest surface area and thus the one for which XRD is most likely to detect OER-induced modifications. The XRD patterns (whose acquisition required ≈30 min) were recorded while holding at $1.0\ V_{RHE}$ before the AST and after 100 or 500 potential cycles, and, as illustrated in Fig. S12, no changes in crystallinity could be inferred from these results.

Complementarily, the occurrence of qualitative changes in the surface morphology of these materials during the AST was investigated via post mortem TEM. As shown in Fig. S13, both of the Nb_2O_5-supported catalysts consist of agglomerated nanocrystals, and it is hard to unambiguously conclude whether any morphologic surface modifications or changes in crystallite size took place in the course of the AST. Specifically, the interplanar distances at multiple locations along the beginning- and end-of-tests catalysts showed no changes after 300 cycles of AST, indicating the structural stability of these materials' surfaces. Alternatively, SEM might be better suited to qualitatively trace surface changes in such agglomerates, and thus, identical location (IL-) SEM was performed before and after the AST to verify the occurrence of modifications in the surface and
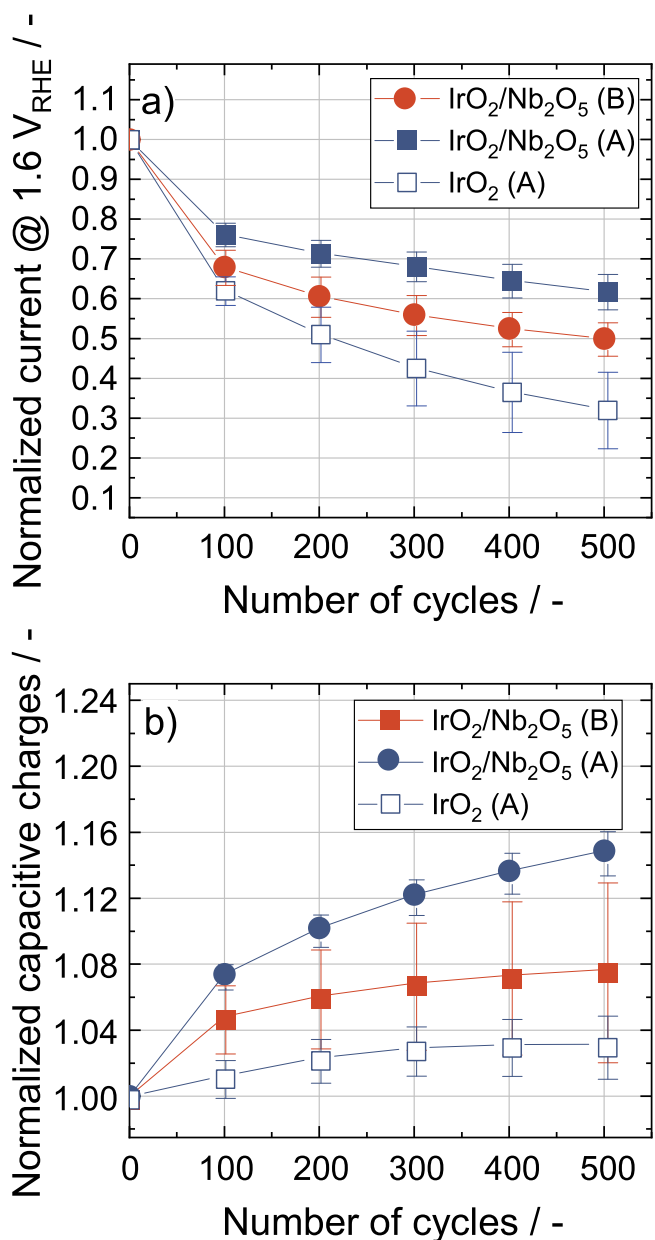
morphology of the same particles. However, the IL-SEM images of the three materials displayed in Fig. S14 show that no morphological differences between specific particles are noticeable before and after the AST. This observation is in line with a previous report[25] in which the absence of morphological differences was however attributed to the low intrinsic resolution of SEM.

On the other hand, IL-SEM images with a lower magnification unveiled that particle migration is visible on all three electrodes. The most distinctive case of this is that of the inhomogeneous IrO_2/Nb_2O_5 (A) sample, in which the Nb_2O_5 particles separated from the IrO_2 phase appear to be prone to detachment upon evolution of O_2 gas on the IrO_2 surfaces below them (see Fig. 6). Notably, this detachment of Nb_2O_5 particles could lead to more IrO_2 surface being exposed to the electrolyte, which would (partially) explain the increase in capacitive charge discussed above (see Fig. 4b), and the related and comparatively smaller loss of current
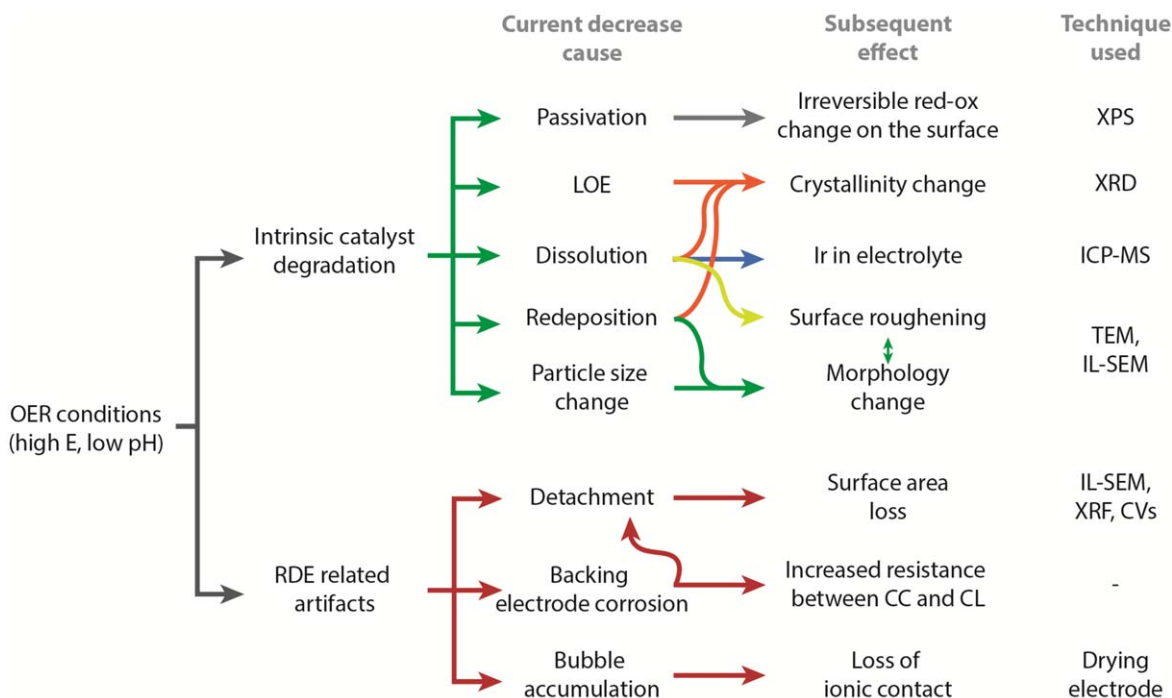
Figure 5. Diagram summarizing the mechanisms that can lead to the OER-current decrease observed in the course of the RDE-ASTs performed in this study. The primary sources of degradation and/or artifacts can be assessed using the techniques listed in the rightmost column. LOE stands for "lattice oxygen evolution," CC for "current collector," and CL for "catalyst layer."

observed for this specific catalyst with regards to the other two samples (cf. Fig. 4a).

Besides for this partial detachment of OER-inactive Nb_2O_5 particles in IrO_2/Nb_2O_5 (A), all materials also exhibited some extent of overall catalyst delamination in the course of the AST, as indicated by the yellow-marked areas in Fig. 6. For all catalysts, some of the material detached from the electrode, exposing new Ir-oxide active areas and/or the glassy the carbon disk used as the backing electrode. Interestingly, this catalyst detachment is systematically accompanied by the re-deposition of some particles, as indicated by the blue-marked areas in Fig. 6. We hypothesize that this migration may stem from an operative deformation of the CLs, in turn caused by mechanical stresses induced by the continuous rotation of the electrodes in the course of the ASTs. Beyond this tentative origin, it appears certain that the migration of particles along the catalyst layer is the dominant process causing the increases of capacitive charge observed in the course of the AST (see Fig. 4b, as opposed to fine changes in the catalysts' surface morphology that could not be discerned through TEM or IL-SEM.

Next, we employed XRF in order to quantify the contribution of the catalyst losses qualitatively discussed above to the observed, AST-induced current decay.[20,68] As discussed in the experimental section, such a quantification is carried out for performing separate XRF measurements on (i) a glassy carbon electrode loaded with the catalyst of interest but not submitted to any electrochemical protocol (referred to as "Before AST"), and (ii) an equivalent electrode having undergone the electrochemical stability protocol (labelled "After AST"). As such, these XRF measurements are not performed on the same electrode, and thus the values inferred from them are representative of absolute catalyst losses (i.e., including both dissolution and delamination) and are affected by the uncertainties in sample loading intrinsic to the preparation of such electrodes, and that we estimate to be ⩽10%. Keeping this in mind, it is worth noting that while the least stable IrO_2 (A) catalyst showed the smallest loss of Ir ($\approx$4%, see Fig. S15), the IrO_2/Nb_2O_5 (B) exhibited an apparent, $\approx$10% gain in Ir mass. These apparent mass changes were reproduced when assessing the Nb-loading (see Fig. S16), whereby the IrO_2/Nb_2O_5 (B) shows a $\approx$7% gain in Nb mass and IrO_2/Nb_2O_5

(A) features a $\approx$14% Nb loss. Since the AST cannot have caused an increase in the Ir-loading, we conclude that the apparent loading differences derived from these XRF results are within the errors associated to the preparation of these electrodes and/or to the procedures followed for technique calibration (see experimental section for details). Thus, we believe that catalyst losses assignable to the partial detachment of the CLs observed in our IL-SEM measurements (*vide supra*) and (to a significantly lesser extent) to the dissolution of the catalysts discussed below remains within the reliability margins of these XRF measurements (i.e., $\approx$10%), and do not significantly contribute to the current decay observed in the AST.

Currently, Ir-dissolution is widely regarded as a major source of degradation for IrO_2-based anodes, and even relatively stable, rutile-type IrO_2 has been shown to dissolve to some extent upon OER.[25,32] In the case of the IrO_2/Nb_2O_5 materials used in this study, both Ir and Nb were detected in the electrolyte after 500 potential cycles (see Fig. 7), with pure IrO_2 dissolving the largest amount of Ir, followed by IrO_2/Nb_2O_5 (A) and IrO_2/Nb_2O_5 (B). These differences in Ir-dissolution among the Nb_2O_5-supported catalysts disagrees with the stability results in Fig. 4a, in which the IrO_2/Nb_2O_5 (A) catalyst features a better stability. Moreover, IrO_2/Nb_2O_5 (B) lost significantly more Nb compared to IrO_2/Nb_2O_5 (A). We note that this behavior does not contradict the results of the IL-SEM measurements discussed above, in which we observed that this IrO_2/Nb_2O_5 (A) catalyst experienced significant detachment of Nb_2O_5 particles, since the latter particles are not detected by the ICP-MS measurements used to quantify Nb-dissolution (which are only sensitive to dissolved ionic species).

Finally, these ICP-MS results can be combined with the catalyst loadings used in these RDE tests to quantify the percentage of Ir and Nb dissolved from the electrodes. Interestingly, this yields a $\approx$2% of Nb loss through dissolution in the case of IrO_2/Nb_2O_5 (A), and approximately $\approx$7% in the case of IrO_2/Nb_2O_5 (B). In contrast, the dissolution of Ir is rather minor for all three catalysts, accounting for $\approx$0.004, $\approx$0.008 and $\approx$0.02% of the Ir-inventory of IrO_2/Nb_2O_5 (B), IrO_2/Nb_2O_5 (A) and IrO_2 (A), respectively. In order to compare the results with literature, one can calculate the corresponding stability (S-) numbers,[65] which are used as indicators of the number of
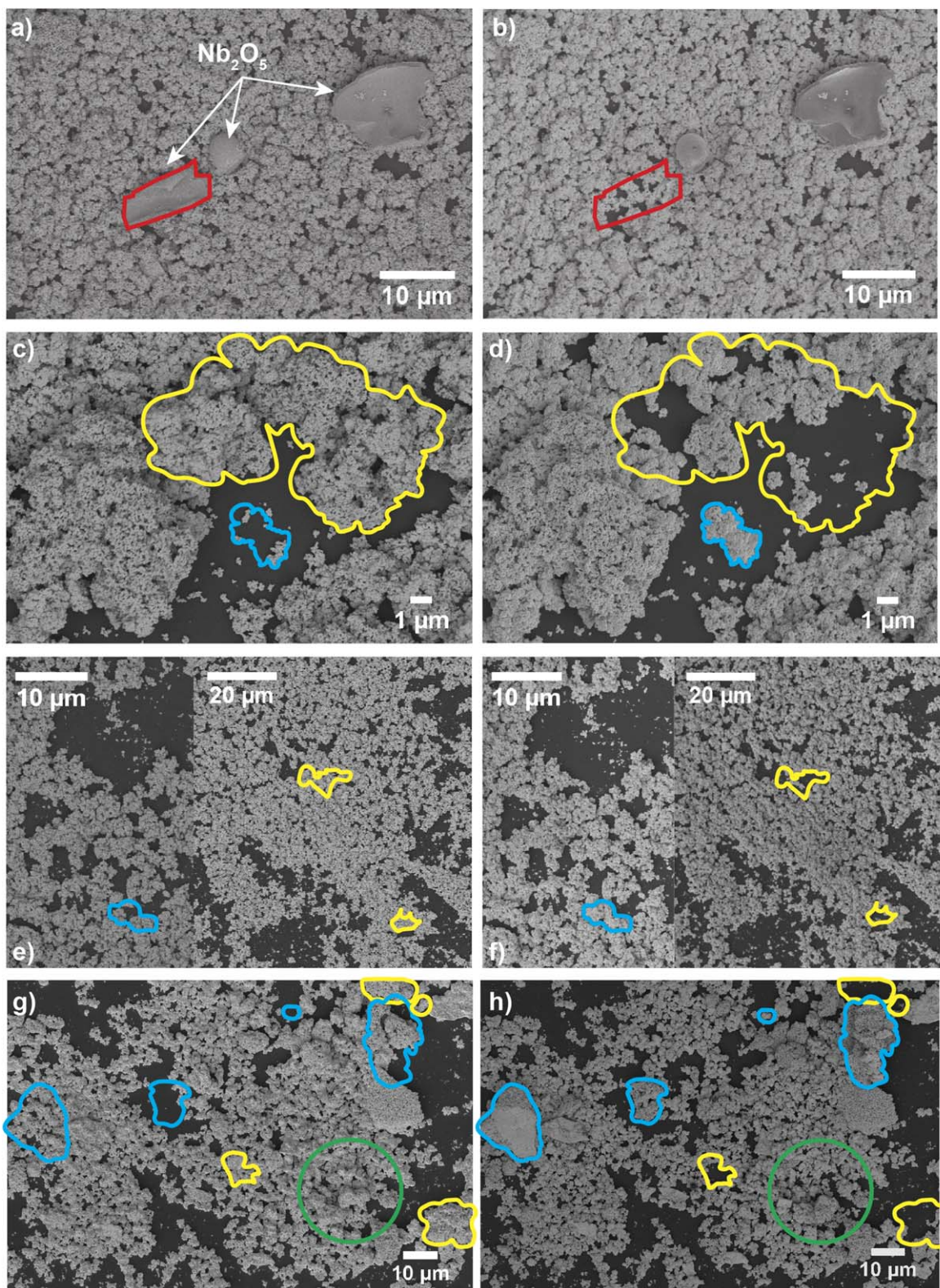
Figure 6. Low magnification IL-SE-micrographs of IrO_2/Nb_2O_5 (A) before (a), (c) and after (b), (d) the AST, showing the detachment of segregated Nb_2O_5 particles (a), (b) as well as general catalyst delamination and re-deposition (c), (d); IL-SEM micrographs before (e), (g) and after (f), (h) the AST for IrO_2/Nb_2O_5 (B) and IrO2 (A), respectively.

evolved oxygen molecules per dissolved Ir atom. As the least stable catalyst, IrO_2 (A) shows the lowest S-number (i.e., $\approx 0.15 \cdot 10^5$), which is an order of magnitude lower than for supported catalysts IrO_2/Nb_2O_5 (A) and IrO_2/Nb_2O_5 (B) (with S-values of $\approx 0.5 \cdot 10^6$ and $1.75 \cdot 10^6$, respectively). The latter values are in line with

previous results reported for rutile IrO_2 catalysts[20,65,69] and Ref., [45] whereby minor Ir dissolution but a significant deactivation of the IrO_2 catalyst after a 2 h hold at $2 \, mA \cdot cm^{-2}$ was also observed. Since we were not able to observe any additional effects of this small extent of Ir dissolution on physicochemical properties that may have
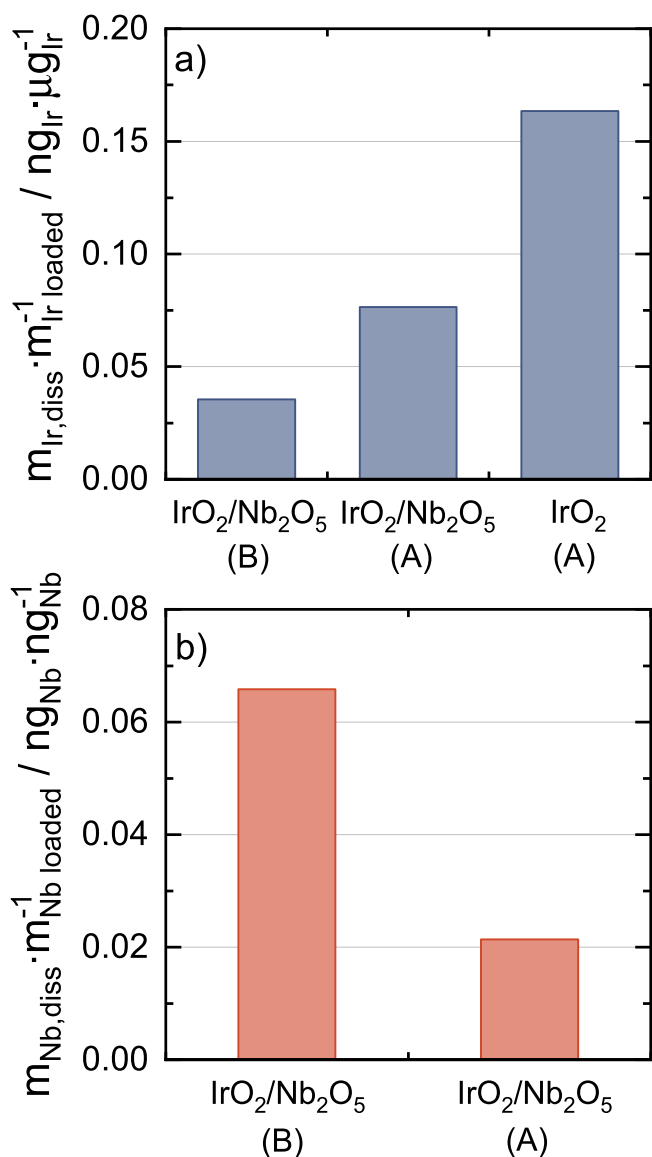
Figure 7. Amounts of Ir (a) and Nb (b) ionic species dissolved in the electrolyte at the end of the AST normalized by the loaded mass on the electrode for the three different catalysts included in this study.

Figure 8. Comparison of the activity losses along the AST for the IrO_2/Nb_2O_5 (B) catalyst using loadings of 100 vs 50 $\mu g_{cat} \cdot$ cm^{-2}, including the normalized current after the electrode with 50 $\mu g_{cat} \cdot$ cm^{2} was dried under vacuum (labelled "after drying") (a) and comparison of the results when Au and GC are used as a substrate for IrO_2/Nb_2O_5 (B) with the same loading of 100 $\mu g_{cat} \cdot$ cm^{-2} (b).

additionally altered the materials' OER-activity (e.g., a change in crystallinity and/or surface roughening—*vide supra*), we conclude that this rather small Ir dissolution cannot explain the significant current decrease observed during the ASTs in Fig. 4a. Based on this investigation of the possible deactivation processes, we cannot fully break down the OER-activity losses undergone by the $IrO_2(/Nb_2O_5)$ catalysts. Therefore, we also investigated possible artifacts that have been reported to compromise the reliability of these RDE measurements when used to assess the stability of OER-catalysts.[46–48] To examine the possible influence of O_2 micro- and nano-bubbles trapped within the pores of the catalyst layer and that would shield its active sites, we repeated the AST on a new electrode of the IrO_2/Nb_2O_5 (B) catalyst using half of the catalyst loading, as to keep the mass-specific current density equal while decreasing the geometrical current density and O_2 production rate[47] (and concomitantly, the chances for gas bubbles to get trapped within the catalyst layer pores). Thus, if such oxygen bubbles were to influence catalyst stability, the activity loss in this measurement with a lower loading should be smaller. However, as shown on Fig. 8a, the current loss is very similar independently of whether a catalyst loading of 50 or 100 $\mu g \cdot$ cm^{-2} is used during the AST, indicating that bubble
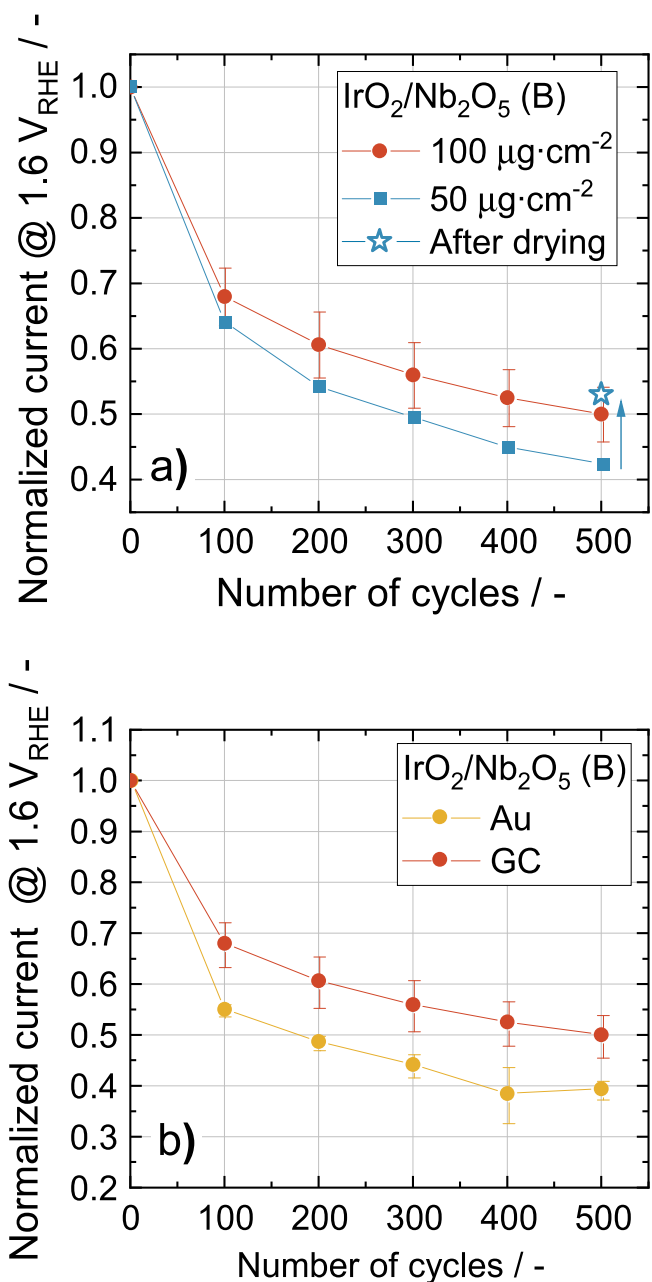
accumulation does not play a major role in this current loss. Additionally, the low-loading electrode having undergone these 500 potential cycles was dried under vacuum ($\approx 10^{-4}$ mbar) as to effectively remove any bubbles that may have remained trapped in the catalyst layer. However, the resulting, dried electrode only displayed a 10% increase in OER-activity, implying again that bubble accumulation only occurs to a small extent and is not responsible for a significant fraction of the activity loss caused by the AST. This is also in line with the literature,[47] where a small effect of bubble accumulation was observed when low mass-specific current densities are applied (as in the case of our ASTs, in which the mass specific currents at the highest potential of 1.6 V_{RHE} were systematically <0.1 mA $\cdot \mu g_{Ir}^{-1}$ for all evaluated catalysts).

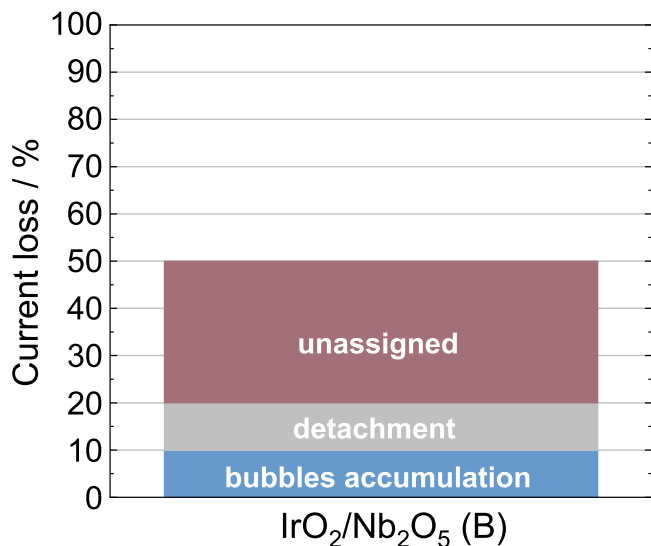**Figure 9.** Breakdown of the contributions of different mechanisms to the overall OER-activity loss undergone by the IrO_2/Nb_2O_5 (B) catalyst in the AST in RDE configuration. Note that the $\approx10\%$ current loss ascribed to catalyst detachment corresponds to a higher estimate based on the XRF-analysis of separate, pre- and post-AST electrodes, and that corresponds to the estimated uncertainty range of the catalyst loading on such electrodes.
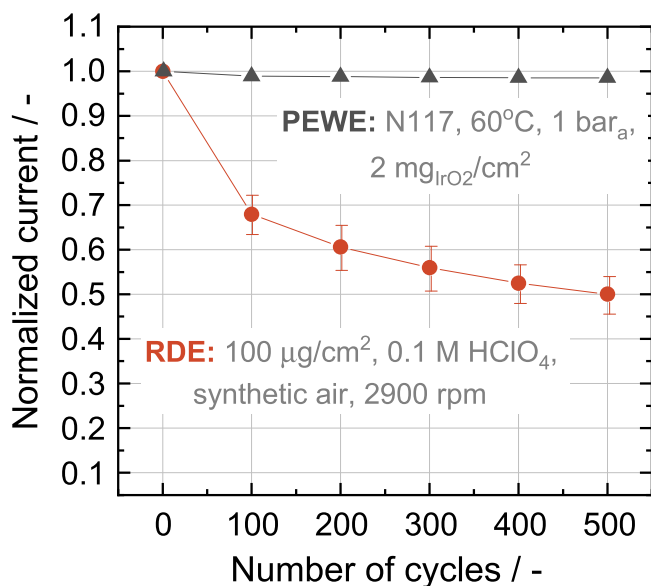

Figure 10. Compared stability of the IrO_2/Nb_2O_5 (B) catalyst in ASTs performed in PEWE vs RDE configurations, whereby the plotted currents are normalized with respect to their beginning-of-test values at 1.6 V_{RHE} in RDE or 1.889 V (cell potential) in the PEWE.

Finally, the current loss observed during the AST could be influenced by the corrosion of the glassy carbon disk used to immobilize the catalysts and as a current collector.[46] However, the maximum potential used during the AST was 1.6 V_{RHE}, and previous studies have reported that exposing glassy carbon to such a potential for 12 h (i.e., 4–fold longer than the duration of our AST) had no significant influence on the activity of the Ir-based material.[46] Instead, much longer times (≈12 d) were required to cause a visible passivation of the glassy carbon at such a "low" potential. Therefore, it is unlikely that glassy carbon corrosion is a significant contributor to the current losses observed during the ASTs. To confirm this hypothesis, we repeated the same AST measurements using poly-crystalline Au instead of glassy carbon as the current collector. As it

can be seen in Fig. 8b, though, the current loss during the AST with Au as a substrate was similar to that observed when glassy carbon was used for this purpose, thus confirming that the electrochemical corrosion of the latter glassy carbon is unlikely to be the source of the observed catalyst degradation.

Given the aforementioned results, we tried to breakdown the current losses undergone during the AST by the IrO_2/Nb_2O_5 (B) catalyst characterized in greater detail. As shown on Fig. 9, out of the 50% total performance decay observed in the AST, equal fractions of $\approx10\%$ can be assigned to catalyst detachment and bubble accumulation, but the larger, remaining 30% of the losses cannot be assigned. Interestingly, it has been reported that ASTs consisting of potential jumps (and thus similar to the one used herein) are more detrimental to catalyst performance than those consisting of potential/current holds or cyclic voltammetry tests.[42,67,70] In this regard, even when using a modified RDE designed to avoid experimental artifacts and isolate bubble accumulation effects, Petzoldt et al.[70] observed irreversible performance degradation only when square wave cycling was used as the OER-stability evaluation protocol. More precisely, the irreversible performance loss observed in that study was $\approx60\%$, and the authors hypothesized that it stemmed from the cycling of Ir between different oxidation states and/or from Ir-dissolution, which was estimated to account for a loss of 0.5% of the initial Ir-inventory on their electrodes. Notably, that value is ≈20-fold greater than the highest ionic Ir-concentration found by us at the end of the ASTs (*vide supra*), and thus we still believe that such Ir-dissolution is not the major source of the current loss observed during our ASTs. Alternatively, El-Sayed et al.[47] also observed that a part ($\approx30\%$) of the irreversible performance loss in their ASTs could not be recovered after Ar purging and, in agreement with ur own observations, the reason for this remained unclear. Thus, if to different extents, our observation that a fraction of the performance losses observed in these RDE-based ASTs cannot be assigned to any of the deactivation mechanism and/or artifacts presented in the literature is fully in line with previous works on this matter.

Beyond these uncertainties, we finalized our work by verifying if this instability is relevant to the implementation of the catalyst in PEWE anodes. To this end, we performed PEWE tests using a stability protocol inspired in the AST applied in the above RDE-measurements and explained in the Experimental section and Supplementary Note 1. Thus, Fig. 10 displays a comparison of the OER-currents in the course of these ASTs (normalized with regards to their beginning-of-test values) in RDE vs PEWE configurations. The higher stability in the latter, application-relevant test is in line with previous literature[71–74] in which the underestimation of the catalyst's lifetime in RDE stability tests was shown to stem from the accumulation of oxygen bubbles in RDE CL-pores[71] and/or from the less acidic environment to which the catalyst is exposed in PEWE tests, which should translate in a lower extent of Ir dissolution.[72] As shown above, though, neither Ir-dissolution nor CL-shielding with bubbles correspond to the major contributors to the current losses in this study's RDE measurements.

Alternatively, one could argue that some of these stability differences may result from the different catalyst loadings used in PEWE vs RDE tests (i.e., ≈2 vs ≈0.075 mg$_{Ir}$ · cm^{-2}, respectively). Specifically, if the same degradation mechanisms are at play in the PEWE and RDE environments, the higher stability observed in the former tests could simply stem from the higher catalyst loading masking the losses and delaying the degradation observed in RDE. In this regard, an enhancement of the durability with higher catalyst loadings in electrolysis configuration has been reported in Ref. 75 (using loadings of 0.4 vs 0.1 mg$_{Ir}$ · cm^{-2}), in which catalyst degradation was ascribed to processes which were not observed here (i.e., significant Ir dissolution, Ir oxidation, particle coalescence and decrease in surface area).[42] Additionally, those differences can also stem from the discrepancies in the initial catalyst structure (i.e., the rutile IrO_2 employed here vs an Ir oxide with a small crystallite size in Ref. 42), as well as from the much

shorter timeframe of our durability measurement (3 vs 525 h).[42] As mentioned above, Petzoldt et al.[70] still observed irreversible degradation in an "artifact free," modified RDE configuration implementing high catalyst loadings (i.e., 2 mg$_{IrO2}$ · cm^{-2}) in combination with AST that consists of sudden potential switches. Therefore, further research efforts are needed to unveil other deactivation mechanisms that currently jeopardize the applicability of such RDE-tests for OER-catalyst stability assessment. For instance, future investigations could focus on monitoring changes in the crystal structure with more surface sensitive technique, as to confirm the structural stability of IrO_2 inferred here on the basis of bulk XRD, post mortem TEM and/or on performing RDE and electrolysis tests with the same catalyst loadings.

Conclusions

In conclusion, we characterized several commercial $IrO_2(/Nb_2O_5)$ catalysts synthesized from different precursors and determined their OER-activity and stability using the RDE-configuration tests extensively applied in this field. These showed that the IrO_2/Nb_2O_5 (B) sample exhibited the highest OER activity compared to IrO_2/Nb_2O_5 (A) and the unsupported IrO_2 (A). On the other hand, the IrO_2/Nb_2O_5 (A) catalyst performed best during the AST, loosing $\approx 40\%$ of its initial current, which nevertheless remains significant for an AST lasting only 3 h.

In order to understand this current loss and the differences among catalysts, a systematic study was carried out in which no deactivation processes relatable to the changes in the Ir active sites were found through post mortem XPS or in situ XRD. On the other hand, the dissolution of both Ir and Nb affecting all catalysts constitutes a minor contribution to the overall current loss during the ASTs. Interestingly, the migration of particles in the catalyst layer across the electrode surface is shown to be a dominant process, with particles detaching, redepositing and rearranging themselves, but no morphological changes, particle growth and/or roughening of the surface due to the dissolution were observed.

Finally, we evaluated the possible impact of known experimental artifacts on the current loss observed during these AST measurements. It was demonstrated that bubble accumulation has a small impact on the observed current decay, since it only accounted for $\approx 10\%$ of it in case of the most OER-active material (i.e., IrO_2/Nb_2O_5 (B)). Complementarily, the influence of glassy carbon corrosion on these instability trends was also excluded based on results presented in the literature, and thus the majority of the current losses (for IrO_2/Nb_2O_5 (B), 30% of the irreversible degradation) could not be assigned. Most importantly, our final comparison with the negligible degradation observed in an equivalent AST carried out in a PEWE cell implies that the durability issues hinted by these RDE tests significantly overestimate the instability of these materials compared to what is observed in application relevant electrolysis cells.

ORCID

Juan Herranz https://orcid.org/0000-0002-5805-6192

References

1. International Renewable Energy Agency, Hydrogen: A renewable energy perspective, IRENA, Abu Dhabi, (2019).
2. B. D. James, D. A. DeSantis, and G. Saur, *Final Report: Hydrogen Production Pathways Cost Analysis (2013 – 2016)*, Strategic Analysis Inc., United States, 2016 (accessed June 24, 2022).
3. US Office of Energy Efficiency and Renewable Energy, *Multi-Year Research, Development, and Demonstration Plan* (accessed June 24, 2022), https://energy.gov/eere/fuelcells/articles/hydrogen-and-fuel-cell-technologies-office-multi-year-research-development.
4. T. Schuler, T. Kimura, T. J. Schmidt, and F. N. Büchi, *Energy Environ. Sci.*, **13**, 2153 (2020).
5. A. Mayyas, M. Ruth, B. Pivovar, G. Bender, and K. Wipke, "Manufacturing Cost Analysis for Proton Exchange Membrane Water Electrolyzers", USDOE National Renewable Energy Laboratory (NREL), United States, https://nrel.gov/docs/fy19osti/72740.pdf, 2019. (accessed June 24, 2022).
6. P. C. K. Vesborg and T. F. Jaramillo, *RSC Adv.*, **2**, 7933 (2012).
7. U. Babic, M. Suermann, F. N. Büchi, L. Gubler, and T. J. Schmidt, *J. Electrochem. Soc.*, **164**, F387 (2017).
8. M. Bernt, C. Schramm, J. Schröter, C. Gebauer, J. Byrknes, C. Eickes, and H. A. Gasteiger, *J. Electrochem. Soc.*, **168**, 084513 (2021).
9. C. Minke, M. Suermann, B. Bensmann, and R. Hanke-Rauschenbach, *Int. J. Hydrogen Energy*, **46**, 23581 (2021).
10. M. Möckl, M. F. Ernst, M. Kornherr, F. Allebrod, M. Bernt, J. Byrknes, C. Eickes, C. Gebauer, A. Moskovtseva, and H. Gasteiger, *J. Electrochem. Soc.*, **169**, 064505 (2022).
11. B. Han, M. Risch, S. Belden, S. Lee, D. Bayer, E. Mutoro, and Y. Shao-Horn, *J. Electrochem. Soc.*, **165**, F813 (2018).
12. C. Comninellis and G. P. Vercesi, "Characterization of DSA-type oxygen evolving electrodes: choice of a coating." *J. Appl. Electrochem.*, **21**, 335 (1991).
13. E. Oakton, D. Lebedev, M. Povia, D. F. Abbott, E. Fabbri, A. Fedorov, M. Nachtegaal, C. Copéret, and T. J. Schmidt, *ACS Catal.*, **7**, 2346 (2017).
14. V. K. Puthiyapura, S. Pasupathi, S. Basu, X. Wu, H. Su, N. Varagunapandiyan, B. Pollet, and K. Scott, *Int. J. Hydrogen Energy*, **38**, 8605 (2013).
15. Q. Feng, X. Z. Yuan, G. Liu, B. Wei, Z. Zhang, H. Li, and H. Wang, *J. Power Sources*, **366**, 33 (2017).
16. C. V. Pham, M. Bühler, J. Knöppel, M. Bierling, D. Seeberger, D. Escalera-López, K. J. J. Mayrhofer, S. Cherevko, and S. Thiele, *Appl. Catalysis B*, **269**, 118762 (2020).
17. G. C. Silva, S. I. Venturini, S. Zhang, M. Löffler, C. Scheu, K. J. J. Mayrhofer, E. A. Ticianelli, and S. Cherevko, *ChemElectroChem*, **7**, 2330 (2020).
18. A. J. Terezo and E. C. Pereira, *Electrochim. Acta*, **45**, 4351 (2000).
19. A. Zlotorowicz, F. Seland, and S. Sunde, *ECS Trans.*, **50**, 71 (2013).
20. C. Spori et al., *ACS Appl. Mater. Interfaces*, **13**, 3748 (2021).
21. U. Babic, M. Tarik, T. J. Schmidt, and L. Gubler, *J. Power Sources*, **451**, 227778 (2020).
22. International Renewable Energy Agency, (2020), Green Hydrogen Cost Reduction: Scaling up Electrolysers to Meet the 1.50C Climate Goal, IRENA, Abu Dhabi.
23. O. Schmidt, A. Gambhir, I. Staffell, A. Hawkes, J. Nelson, and S. Few, *Int. J. Hydrogen Energy*, **42**, 30470 (2017).
24. C. C. McCrory, S. Jung, J. C. Peters, and T. F. Jaramillo, *J. Am. Chem. Soc.*, **135**, 16977 (2013).
25. P. Jovanovic et al., *J. Am. Chem. Soc.*, **139**, 12837 (2017).
26. A. Weiß, A. Siebel, M. Bernt, T. H. Shen, V. Tileli, and H. A. Gasteiger, *J. Electrochem. Soc.*, **166**, F487 (2019).
27. N. Danilovic et al., *J. Phys. Chem. Lett.*, **5**, 2474 (2014).
28. S. Cherevko, O. Kasian, N. Kulyk, J. P. Grote, A. Savan, B. R. Shrestha, S. Merzlikin, B Breitbach, A. Ludwig, and K. J. J. Mayrhofer, *Catal. Today*, **262**, 170 (2016).
29. S. Geiger, O. Kasian, B. R. Shrestha, A. M. Mingers, K. J. J. Mayrhofer, and S. Cherevko, *J. Electrochem. Soc.*, **163**, F3132 (2016).
30. S. Cherevko, S. Geiger, O. Kasian, A. Mingers, and K. J. J. Mayrhofer, *J. Electroanal. Chem.*, **774**, 102 (2016).
31. S. Cherevko, S. Geiger, O. Kasian, A. Mingers, and K. J. J. Mayrhofer, *J. Electroanal. Chem.*, **773**, 69 (2016).
32. O. Kasian, J. P. Grote, S. Geiger, S. Cherevko, and K. J. J. Mayrhofer, *Angew. Chem. Int. Ed. Engl.*, **57**, 2488 (2018).
33. T. Binninger, R. Mohamed, K. Waltar, E. Fabbri, P. Levecque, R. Kotz, and T. J. Schmidt, *Sci. Rep.*, **5**, 12167 (2015).
34. O. Kasian et al., *Energy Environ. Sci.*, **12**, 3548 (2019).
35. K. Schweinar, B. Gault, I. Mouton, and O. Kasian, *J. Phys. Chem. Lett.*, **11**, 5008 (2020).
36. D. F. Abbott, D. Lebedev, K. Waltar, M. Povia, M. Nachtegaal, E. Fabbri, C. Copéret, and T. J. Schmidt, *Chem. Mater.*, **28**, 6591 (2016).
37. T. Li, O. Kasian, S. Cherevko, S. Zhang, S. Geiger, C. Scheu, P. Felfer, D. Raabe, B. Gault, and K. J. J. Mayrhofer, *Nat. Catal.*, **1**, 300 (2018).
38. M. Povia et al., *Energy Environ. Sci.*, **12**, 3038 (2019).
39. H. Yu, N. Danilovic, Y. Wang, W. Willis, A. Poozhikunnath, L. Bonville, C. Capuano, K. Ayers, and R. Maric, *Appl. Catalysis B*, **239**, 133 (2018).
40. X. Tan, J. Shen, N. Semagina, and M. Secanell, *J. Catal.*, **371**, 57 (2019).
41. F. Claudel, L. Dubau, G. Berthomé, L. Sola-Hernandez, C. Beauger, L. Piccolo, and F. Maillard, *ACS Catal.*, **9**, 4688 (2019).
42. S. M. Alia, K. S. Reeves, H. Yu, J. Park, N. Kariuki, A. J. Kropf, D. J. Myers, and D. A. Cullen, *J. Electrochem. Soc.*, **169**, 054517 (2022).
43. C. Spori, J. T. H. Kwan, A. Bonakdarpour, D. P. Wilkinson, and P. Strasser, *Angew. Chem. Int. Ed. Engl.*, **56**, 5994 (2017).
44. S. Siracusano, V. Baglio, A. Stassi, R. Ornelas, V. Antonucci, and A. S. Aricò, *Int. J. Hydrogen Energy*, **36**, 7822 (2011).
45. I. Spanos, A. A. Auer, S. Neugebauer, X. Deng, H. Tüysüz, and R. Schlögl, *ACS Catal.*, **7**, 3768 (2017).
46. S. Geiger, O. Kasian, A. M. Mingers, S. S. Nicley, K. Haenen, K. J. J. Mayrhofer, and S. Cherevko, *ChemSusChem*, **10**, 4140 (2017).

47. H. A. El-Sayed, A. Weiß, L. F. Olbrich, G. P. Putro, and H. A. Gasteiger, *J. Electrochem. Soc.*, **166**, F458 (2019).
48. A. Hartig-Weiss, M. F. Tovini, H. A. Gasteiger, and H. A. El-Sayed, *ACS Appl. Energy Mater.*, **3**, 10323 (2020).
49. T. Binninger, E. Fabbri, A. Patru, M. Garganourakis, J. Han, D. F. Abbott, O. Sereda, R. Kötz, A. Menzel, and M. Nachtegaal, *J. Electrochem. Soc.*, **163**, H906 (2016).
50. N. Diklić, A. H. Clark, J. Herranz, J. S. Diercks, D. Aegerter, M. Nachtegaal, A. Beard, and T. J. Schmidt, *ACS Energy Lett.*, **7**, 1735 (2022).
51. S. Garbe, J. Futter, T. J. Schmidt, and L. Gubler, *Electrochim. Acta*, **377**, 138046 (2021).
52. S. Garbe, J. Futter, A. Agarwal, M. Tarik, A. A. Mularczyk, T. J. Schmidt, and L. Gubler, *J. Electrochem. Soc.*, **168**, 044515 (2021).
53. A. Pătru, A. Rabis, S. E. Temmel, R. Kotz, and T. J. Schmidt, *Catal. Today*, **262**, 161 (2016).
54. B. Pribyl-Kranewitter, A. Beard, T. Schuler, N. Diklić, and T. J. Schmidt, *J. Electrochem. Soc.*, **168**, 043506 (2021).
55. D. A. Shirley, *Physical Review B*, **5**, 4709 (1972).
56. V. Pfeifer et al., *Surf. Interface Anal.*, **48**, 261 (2016).
57. M. A. Aegerter, *Solar Energy Materials & Solar Cells*, **68**, 401 (2001).
58. R. J. Cava, B. Batlogg, J. J. Krajewski, H. F. Poulsen, P. Gammel, W. F. Peck, and L. W. Rupp Jr Jr, *Phys. Rev. B: Condens. Matter*, **44**, 6973 (1991).
59. E. Oakton, D. Lebedev, A. Fedorov, F. Krumeich, J. Tillier, O. Sereda, T. J. Schmidt, and C. Copéret, *New J. Chem.*, **40**, 1834 (2016).
60. G. Greczynski and L. Hultman, *Prog. Mater Sci.*, **107**, 100591 (2020).
61. S. Ardizzone, A. Carugati, and S. Trasatti, *J. Electroanal. Chem.*, **126**, 287 (1981).
62. C. Felix, B. Bladergroen, V. Linkov, B. Pollet, and S. Pasupathi, *Catalysts*, **9**, 318 (2019).
63. J. Durst, A. Siebel, C. Simon, F. Hasché, J. Herranz, and H. A. Gasteiger, *Energy Environ. Sci.*, **7**, 2255 (2014).
64. J. Durst, C. Simon, F. Hasché, and H. A. Gasteiger, *J. Electrochem. Soc.*, **162**, F190 (2014).
65. S. Geiger et al., *Nat. Catal.*, **1**, 508 (2018).
66. V. A. Saveleva, L. Wang, D. Teschner, T. Jones, A. S. Gago, K. A. Friedrich, S. Zafeiratos, R. Schlogl, and E. R. Savinova, *J. Phys. Chem. Lett.*, **9**, 3154 (2018).
67. C. Spöri, C. Brand, M. Kroschel, and P. Strasser, *J. Electrochem. Soc.*, **168**, 034508 (2021).
68. M. Chourashiya, R. Sharma, and S. M. Andersen, *Anal. Chem.*, **90**, 14181 (2018).
69. S. Czioska et al., *ACS Catal.*, **11**, 10043 (2021).
70. P. J. Petzoldt, J. T. H. Kwan, A. Bonakdarpour, and D. P. Wilkinson, *J. Electrochem. Soc.*, **168**, 026507 (2021).
71. M. Fathi Tovini, A. Hartig-Weiß, H. A. Gasteiger, and H. A. El-Sayed, *J. Electrochem. Soc.*, **168**, 014512 (2021).
72. J. Knoppel, M. Mockl, D. Escalera-Lopez, K. Stojanovski, M. Bierling, T. Bohm, S. Thiele, M. Rzepka, and S. Cherevko, *Nat. Commun.*, **12**, 2231 (2021).
73. K. Ehelebe, D. Escalera-López, and S. Cherevko, *Current Opinion in Electrochemistry*, **29**, 100832 (2021).
74. S. M. Alia, M.-A. Ha, G. C. Anderson, C. Ngo, S. Pylypenko, and R. E. Larsen, *J. Electrochem. Soc.*, **166**, F1243 (2019).
75. S. M. Alia, S. Stariha, and R. L. Borup, *J. Electrochem. Soc.*, **166**, F1164 (2019).